

# MIRAM: Masked Image Reconstruction Across Multiple Scales for Breast Lesion Risk Prediction

Hung Q. Vo<sup>†</sup>, Pengyu Yuan<sup>†</sup>, Zheng Yin<sup>‡</sup>, Kelvin K. Wong<sup>‡</sup>,  
Chika F. Ezeana<sup>‡</sup>, Son T. Ly<sup>†</sup>, Stephen T.C. Wong<sup>†</sup> and Hien V. Nguyen<sup>‡</sup>

<sup>†</sup>Department of Electrical and Computer Engineering, University of Houston

<sup>‡</sup>Systems Medicine and Biomedical Engineering, Houston Methodist

**Abstract**—Self-supervised learning (SSL) has garnered substantial interest within the machine learning and computer vision communities. Two prominent approaches in SSL include contrastive-based learning and self-distillation utilizing cropping augmentation. Lately, masked image modeling (MIM) has emerged as a more potent SSL technique, employing image inpainting as a pretext task. MIM creates a strong inductive bias toward meaningful spatial and semantic understanding. This has opened up new opportunities for SSL to contribute not only to classification tasks but also to more complex applications like object detection and image segmentation. Building upon this progress, our research paper introduces a scalable and practical SSL approach centered around more challenging pretext tasks that facilitate the acquisition of robust features. Specifically, we leverage multi-scale image reconstruction from randomly masked input images as the foundation for feature learning. Our hypothesis posits that reconstructing high-resolution images enables the model to attend to finer spatial details, particularly beneficial for discerning subtle intricacies within medical images. The proposed SSL features help improve classification performance on the Curated Breast Imaging Subset of Digital Database for Screening Mammography (CBIS-DDSM) dataset. In pathology classification, our method demonstrates a 3% increase in average precision (AP) and a 1% increase in the area under the receiver operating characteristic curve (AUC) when compared to state-of-the-art (SOTA) algorithms. Moreover, in mass margins classification, our approach achieves a 4% increase in AP and a 2% increase in AUC.

**Index Terms**—Self-supervised Learning, Vision Transformer, Breast Cancer, Mammogram.

## I. INTRODUCTION

The scarcity of annotated data poses a significant challenge in the application of deep learning within medical settings. The annotation process for medical images is typically expensive and relies on expert knowledge, creating a bottleneck that hampers progress in the field. In contrast, there is a wealth of unannotated medical data available from hospitals and medical institutions. However, conventional supervised deep learning methods are unable to leverage the potential of such invaluable data sources. Self-supervised learning (SSL) offers a promising framework for acquiring powerful features without the need for annotated data. SSL models excel at learning meaningful features by exploiting the inherent data structure or the underlying relationships between different modalities, such as videos and audios. The application of SSL

has sparked innovation in various medical image domains, including dermatology diseases, chest X-ray pathologies, and digital whole slide images [1] [2].

Multiple works have leveraged SSL for breast cancer diagnosis on MGs. In [3], SSL together with weakly-supervised learning are used for abnormality detection in MGs. By using benign images perturbed by synthetically generated artifacts as training data, an autoencoder can be trained to separate abnormal from normal regions and into two separate channels. Our work also uses an autoencoder for SSL pre-training; however, we focus on lesion risk analysis where tiny details of a lesion must be carefully inspected. In clinical workflow, this analysis usually occurs at a later stage after abnormalities in an MG have been localized by radiologists.

Several studies have utilized self-supervised learning (SSL) in the context of breast cancer diagnosis using mammograms (MG). In the work by Perek et al. [4], SSL contrastive learning was applied to both whole-MG and ultrasound classifications. Another study by Miller et al. [5] concentrated on whole-MG classification but employed lesion-level image patches for pre-training. Although the paper includes evaluations for lesion-level patch classification, the results are limited and lack in-depth insights.

In our research paper, we conduct a comprehensive analysis of self-supervised learning (SSL) for lesion-level classification. Our primary emphasis lies in exploring transformer architectures, known for scaling well with large amounts of pre-training data. This is particularly advantageous in SSL, as it eliminates the need for annotations. Additionally, we introduce a novel pretext task called multi-scale reconstruction, which involves the reconstruction of images at multiple scales.

Within the realm of self-supervised learning (SSL), contrastive learning [6] and self-distillation [7] have emerged as the dominant approaches. However, their success comes from the idea of encouraging features of different augmented crops from a single image close together, which makes learned features invariant to scaling and shifting. Consequently, learned features are useful for classification but not other downstream tasks such as detection or segmentation.

The masked auto-encoder (MAE), another image-based SSL approach that came later [8], has demonstrated superior classification performance, surpassing even supervised settings in detection and segmentation tasks. The concept behind MAE is straightforward: the pretext task involves reconstructing an

\* Corresponding email: hqvo2@uh.edu

\*\* Hien V. Nguyen and Stephen T.C. Wong are co-senior authors

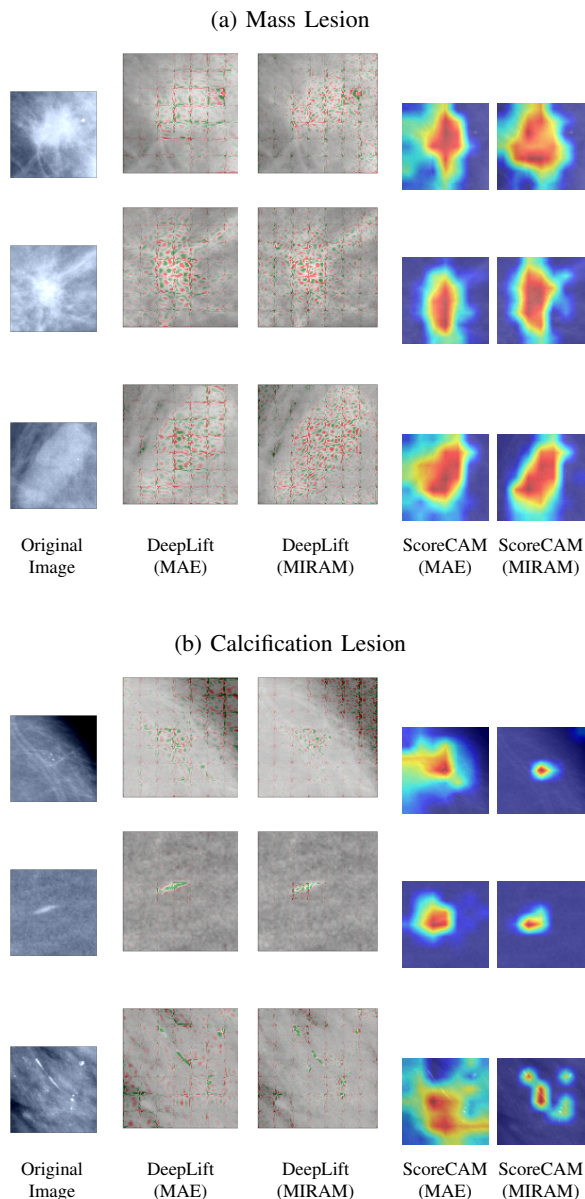


Fig. 1: Visualization of Learned Features on Pathology Classification Task. Our proposed MIRAM method shows improvements over the original MAE in terms of localizing the lesion’s region and capturing finer details.

incomplete image, compelling the model to comprehend the image and recover the missing regions. Building upon this idea, we propose the use of multi-scale image inpainting as a novel pretext task. Unlike MAE, which employs image inpainting at a single scale, our approach involves reconstructing images at multiple scales. Experimental results reveal that this more challenging pretext task enhances the model’s performance in downstream classification tasks. Additionally, the reconstruction of high-resolution images has enabled the model to focus on smaller yet more intricate spatial details (see Figure 1).

The MIRAM (Masked Image Reconstruction Across Multiple Scales) approach consistently demonstrates favorable

outcomes across various breast lesion risk prediction tasks. The methodology involves pre-training the model on multiple mammogram (MG) datasets and subsequently fine-tuning it for the specific downstream task. Notably, in the case of pathology classification on the CBIS-DDSM dataset, our proposed method achieves a notable enhancement of 3% in average precision (AP) and 1% in the area under the receiver operating characteristic curve (AUC). Similarly, for mass margins multi-label classification, MIRAM exhibits improvements of 4% in AP and 2% in AUC.

## II. METHODOLOGY

### A. MIRAM

1) *General Idea:* Building upon the achievements of Masked Autoencoders (MAE) [8], our proposed approach involves training this generative-based self-supervised learning (SSL) model with a novel pretext task: multi-scale image reconstruction. By introducing this more demanding task, we aim to facilitate the acquisition of more informative features by the model. Additionally, employing high-resolution image reconstruction tasks allows the model to effectively capture finer spatial details, as illustrated in Figure 1.

The Vision Transformer (ViT) architecture operates on an input image, denoted as  $x$ , where  $x \in \mathbb{R}^{n \times n}$ . Initially, the image is evenly divided into  $L$  smaller patches, represented as  $(x_{P_1}, \dots, x_{P_L}) \in \mathbb{R}^{L \times p \times p}$ , with  $p = n/\sqrt{L}$  indicating the patch size. These individual patches also referred to as tokens, are then processed through multiple self-attention blocks to capture their inherent relationships. One notable advantage of the transformer architecture compared to convolutional neural networks (CNNs) is its explicit modeling of global relationships among tokens. While CNNs encode the entire image into a single vector, transformers encode each image patch into a distinct vector while simultaneously capturing the relationships among all the patches. This characteristic makes transformers well-suited for masked image modeling tasks.

Taking advantage of the architectural benefits of Vision Transformers (ViT), the MAE (Masked Autoencoder) approach [8] employs image inpainting as a self-supervised learning (SSL) pretext task to pre-train the token representations. In this process, a substantial portion of input patches is randomly masked, and only the unmasked portions are fed into the transformer encoder. The encoded representations of these non-masked tokens are then passed through the transformer decoder to reconstruct the original image. By employing the image inpainting pretext task, the ViT encoder is guided to learn meaningful representations of the non-masked tokens, enabling the model to predict the missing patches (masked tokens) effectively.

While the Vision Transformer (ViT) architecture has its advantages, it is known to have limitations in capturing fine spatial details due to its fixed token patch size and constant number of tokens across multiple self-attention blocks [9]. To address this limitation, we introduce a more challenging pretext task in our work: multi-scale images reconstruction. By employing high-resolution image reconstruction as a pretext

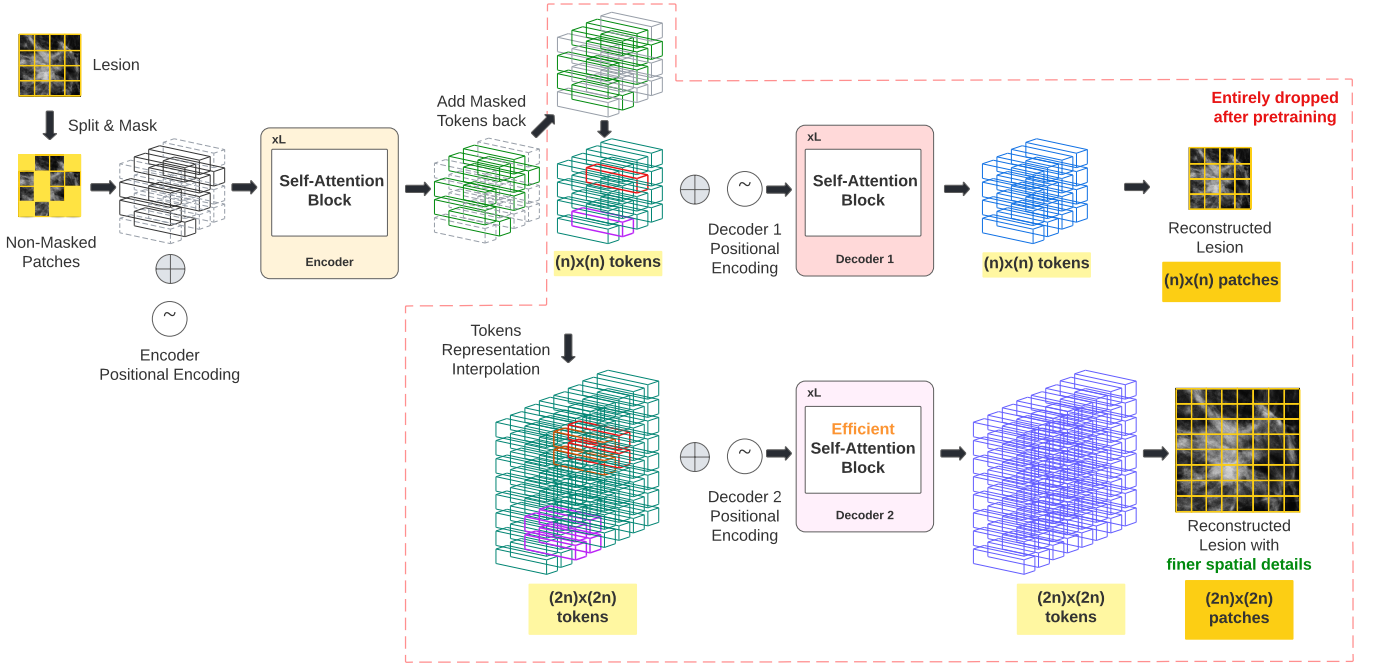


Fig. 2: The MIRAM SSL Framework: Two different scales are reconstructed – one for the original size, while the other is twice the size of both the original height and width.

task, we aim to guide our model to learn more fine-grained features. This approach has the potential to encourage the model to focus on finer spatial details, as illustrated in Figure 1.

To enable multiscale image reconstruction, we build upon the original decoder architecture of the Masked Autoencoder (MAE) [8] with a straightforward modification. In MAE, a decoder is used to reconstruct the original image following the encoder. In our approach, we extend this framework by incorporating multiple decoders, each decoder being responsible for handling a specific scale. Consequently, a separate reconstruction loss is computed for each decoder, capturing the fidelity of the reconstructed image at its respective scale. To form the total loss, we simply take the average of all the individual reconstruction losses, ensuring that each scale contributes equally to the overall training objective.

The inclusion of multiple decoders in our proposed approach allows for the reconstruction of larger images by increasing the number of tokens fed into the decoder. This expanded input capacity potentially enables the decoder to attend to finer spatial details when reconstructing high-resolution images. In our work, we introduce an additional decoder for each additional scale we aim to reconstruct, in addition to the original one. While it is possible in theory for a single decoder to handle multiple scales, we follow the approach of ViT [10], where the transformer model demonstrates improved performance when trained with fixed-resolution images. Thus, we employ a single decoder for each scale, maintaining the benefits of fixed-resolution training as observed in the ViT architecture.

Each patch  $x_{P_i}$  is considered a token of this image and

their embeddings  $(e_{P_1}, \dots, e_{P_L}) \in \mathbb{R}^{L \times D}$  ( $D$  is the selected embedding dimension), are first obtained through patch embedding layer [10]. These input embeddings  $(e_{P_1}, \dots, e_{P_L})$  are then fed through a sequence of self-attention blocks to learn the relationships among these tokens. A new state of these embeddings  $(\tilde{e}_{P_1}, \dots, \tilde{e}_{P_L}) \in \mathbb{R}^{L \times D}$  is obtained where the number of tokens  $L$  and token features dimensions  $D$  are fixed through a sequence of self-attention blocks.

$$(\tilde{e}_{P_1}, \dots, \tilde{e}_{P_L}) = ViT(x) = ViT((e_{P_1}, \dots, e_{P_L})) \quad (1)$$

Only after encoding stage, masked tokens embeddings  $(e_{P_1}^\psi, \dots, e_{P_{L-K}}^\psi) \in \mathbb{R}^{(L-K) \times D}$  are added back to form the full tokens embeddings  $(\tilde{e}_{P_1}, \dots, \tilde{e}_{P_L}) \in \mathbb{R}^{L \times D}$  which are then fed into the decoder for whole image reconstruction. Let  $(e_{P_1}^\phi, \dots, e_{P_K}^\phi) \in \mathbb{R}^{K \times D}$  be the embeddings of remaining non-masked tokens:

$$(\tilde{e}_{P_1}^\phi, \dots, \tilde{e}_{P_K}^\phi) = ViT(x) = ViT((e_{P_1}^\phi, \dots, e_{P_K}^\phi)) \quad (2)$$

$$(\tilde{e}_{P_1}, \dots, \tilde{e}_{P_L}) = deshuffle(\{\tilde{e}_{P_1}^\phi, \dots, \tilde{e}_{P_K}^\phi, e_{P_1}^\psi, \dots, e_{P_{L-K}}^\psi\}) \quad (3)$$

By using ViT, the masking tokens process is straightforward to implement [8]. After getting back the full tokens embeddings  $(\tilde{e}_{P_1}, \dots, \tilde{e}_{P_L}) \in \mathbb{R}^{L \times D}$ , MAE fed them into the decoder for reconstructing the original image. Let  $\hat{x} \in \mathbb{R}^{n \times n}$  be the reconstructed image:

$$\hat{x}_1 = Decoder_1((\tilde{e}_{P_1}, \dots, \tilde{e}_{P_L})) \quad (4)$$

In this work, we include an additional decoder for handling fine details reconstruction tasks. This decoder focuses on reconstructing the finer spatial details of the image. Although one can use only one decoder for both tasks as the transformer model was originally developed for training on sequences of different lengths [11]. Here, we follow the ViT [10], where the transformer is trained with fixed-resolution images.

2) *Encoded Tokens Interpolation*: To address the fixed number of encoded tokens for reconstructing higher-scale images, we propose feature interpolation. By interpolating features, we generate additional tokens for the higher-scale decoders, capturing finer details effectively. This approach enhances representation capacity and accommodates varying levels of detail across scales.

We employ a straightforward duplicate interpolation method. In this method, for each encoded token, we interpolate the missing neighboring tokens by duplicating the selected token’s feature vector. While alternative interpolation methods could be considered, we opt for simplicity to encourage the encoder to focus on learning robust token representations rather than relying heavily on a sophisticated upsampling process. For a visual representation of the entire interpolation process, please refer to Figure 2.

However, as the original task is only to reconstruct the original image  $x \in \mathbb{R}^{n \times n}$ , the numbers of tokens  $L$  being fed to the decoder are the same with that when the original image was split. To increase the numbers of tokens for feeding into our new fine-spatial decoder, we use duplicate interpolation. Specifically, for each token embeddings from encoded tokens, we simply interpolate missing neighbors by copying the selected token embedding. This interpolation is not only simple and efficient but also effective for SSL training representations and is referred in our paper as useful “tokens bottleneck”. Specifically, let select a token embedding  $\tilde{e}_{P_1} \in \mathbb{R}^D$ . In the original decoder,  $\tilde{e}_{P_1}$  is used as main information to reconstruct the patch  $x_{P_1} \in \mathbb{R}^{p \times p}$  of the original image. For feeding into our new decoder,  $\tilde{e}_{P_1}$  is first duplicated  $k$  times to handle  $k$  separate sub-regions of the same patch  $x_{P_1}$ . In this paper,  $k$  is set to 4 for double both the width and height of the reconstruction image. Because all duplicated embeddings of  $\tilde{e}_{P_1}$  have the same features representation but is used to reconstruct different sub-regions of  $x_{P_1}$ , this process is named “tokens bottleneck”. Let  $\tilde{e}_{duplicate} \in \mathbb{R}^{kL \times D}$  be the duplicated tokens embeddings and let  $\hat{x}_2 \in \mathbb{R}^{(k/2)n \times (k/2)n}$  be the reconstructed image with higher resolution, the entire process is formulated as below:

$$\begin{aligned} \tilde{e}_{duplicate} &= \text{duplicate}(\tilde{e}_{P_1}, \dots, \tilde{e}_{P_L}; k) \\ &= (\tilde{e}_{P_1^1}, \dots, \tilde{e}_{P_1^k}, \dots, \tilde{e}_{P_L^1}, \dots, \tilde{e}_{P_L^k}) \end{aligned} \quad (5)$$

$$\hat{x}_2 = \text{Decoder}_2(\tilde{e}_{duplicate}) \quad (6)$$

Making the interpolation as simple as possible, we want the encoder to learn strong tokens embeddings instead of learning some powerful upsampling process. For the same purpose, we also make our second decoder as simple as possible.

Precisely, our second decoder has the same architecture as the first decoder (with the same numbers of self-attention blocks, the same numbers of heads, the same embedding dimension). Consequently, for the reconstruction process to be successful, tokens representations must learn something meaningful instead of having a powerful decoder.

3) *Linear self-attention for long-range sequences*: To address the computational complexity associated with capturing finer details in high-resolution image reconstruction, we explore alternatives to the quadratic self-attention present in traditional transformer models. The quadratic complexity arises from the dependence on the number of tokens, resulting in significant time and memory consumption. In this paper, we investigate the feasibility of using linear self-attention algorithms as approximations to the standard self-attention mechanism. Specifically, we experiment with three linear self-attention algorithms: Linformer [12], Performer [13], and Nystromformer [14]. While these algorithms have primarily been evaluated in natural language processing (NLP) tasks, we explore their applicability in the context of image analysis. The results and comparisons of these linear self-attention algorithms are discussed in detail in the experimental section of our paper.

## B. SS Pre-training Stage

During the pre-training stage, we adhere closely to the methodology outlined in the original MAE paper by He et al. [8], where the model is trained to reconstruct the original image. However, in our paper, we introduce a more challenging objective, namely the reconstruction of multi-scale images. By adopting this harder pretext task, we aim to facilitate more effective feature learning. This approach encourages the model to capture finer details when reconstructing high-resolution images, potentially leading to the acquisition of more powerful features. Through our experiments, we demonstrate that the inclusion of this harder pretext task enhances the model’s feature learning capabilities. Quantitative improvement is shown in table III and table IV. Qualitative improvement is shown in figure ??.

In the MAE framework introduced by He et al. [8], the image reconstruction process involves an encoder followed by a decoder. However, in our proposed approach, we extend the architecture to accommodate the reconstruction of multiple scales. Specifically, we incorporate  $j$  decoders, each responsible for reconstructing a single scale. Consequently, we have  $j$  separate reconstruction losses, denoted as  $J_I$ . To combine these losses, we employ an equally weighted average, ensuring each scale contributes equally to the overall reconstruction objective. This adaptation allows us to handle multi-scale image reconstruction within our framework effectively.

To compute the image reconstruction loss  $J_I$ , we follow the methodology described in the MAE paper by He et al. [8]. Initially, we calculate the reconstruction losses  $J_P$  for all reconstructed patches  $\hat{P}$  using the mean squared error. These individual patch reconstruction losses capture the discrepancy between the reconstructed patches and the corresponding

ground truth patches. Subsequently, the image reconstruction loss  $J_I$  is formed by taking the average of all  $L$  patch reconstruction losses, as outlined in Equation 7. This approach ensures that the overall image reconstruction loss effectively measures the fidelity of the reconstructed image.

$$J_P = \frac{1}{p * p} \sum_{i=1}^{p*p} (\hat{P}_i - P_i)^2; \quad J_I = \frac{1}{L} \sum_{l=1}^L J_{P_l} \quad (7)$$

Following the pre-training stage, we proceed with fine-tuning the pre-trained model weights for various downstream tasks. While it is common to employ both Linear Probing and Fine-tuning of the entire model to evaluate learned SSL representations [6], [8], we solely focus on Fine-tuning in our experiments. This decision is motivated by the observation that the representations learned by MAE are characterized by strong non-linear features but may exhibit less linear separability [8]. Therefore, we choose to exclusively utilize Fine-tuning as our evaluation approach to leverage the model’s non-linear capabilities in capturing complex patterns and features.

### III. DATASETS

We carefully selected diverse datasets for our study, which encompass different origins and include both film and digital mammograms. Given the specific focus of our paper on breast lesion analysis, datasets with lesion-level annotations are of utmost importance to us. We prioritize the use of the following datasets in our experiments: INbreast [15], BCDR [16], CBIS-DDSM [17], and CSAW-S [18]. These datasets offer valuable resources for evaluating and validating our proposed approach in the context of breast lesion analysis. In line with the findings of Shen et al. [19], which highlighted the importance of utilizing both lesion crops and random background crops in the learning process, we adopt a similar approach in our SSL pre-training stage. While data with lesion-level annotations is limited, we aim to leverage additional datasets that offer image-level annotations. Specifically, we incorporate the CSAW-M dataset [20] and the CMMD dataset [21] into our pre-training process. For these datasets, we employ random crops from the mammograms, allowing for the possibility of capturing the presence of lesions. By incorporating both types of crops, we aim to enhance the learning process and enable the model to effectively capture relevant features for lesion analysis.

1) *For pre-training stage:* Three different combinations of datasets for the SSL pre-training stage are: 1) CBIS-DDSM with ground-truth crops (CBIS-DDSM), 2) All datasets with ground-truth crops (Lesions Only), and 3) Lesion-Level datasets with ground-truth crops + Image-Level datasets with random crops (MGs & Lesions). Further analysis and comparison of performance across various pre-trained datasets will be discussed in detail in the experiment section.

2) *For downstream classification tasks:* Our evaluation primarily centers around CBIS-DDSM, a widely utilized publicly available mammogram dataset in previous studies [19] [22]. We specifically focus on two evaluation tasks: pathology

classification (with 4 classes: benign mass, malignant mass, benign calcification, and malignant calcification) and mass margins classification.

## IV. EXPERIMENTAL RESULTS

### A. Experimental Setup and Evaluation Metrics

1) *Architecture Setup:* In our MIRAM approach, we conduct experiments using two different reconstruction scales (as depicted in Figure 2). The first scale corresponds to the original size of  $112 \times 112$ , while the second scale involves higher-resolution reconstruction with dimensions of  $224 \times 224$ , which is twice the size of both the original height and width. To facilitate this multi-scale reconstruction, we employ two separate decoders: the *original* decoder and the *high-resolution* decoder.

2) *Training Setup:* Our experimental process consists of two main stages: SSL pre-training and fine-tuning on a downstream task. During pre-training, we explore different MG datasets, while for the downstream classification, we specifically focus on pathology classification and mass margins multi-label classification tasks. All reported results are obtained using the official test set of CBIS-DDSM. In the pre-training stage, the model undergoes 500 epochs of training on one of the selected combinations of MG datasets. Subsequently, the pre-trained weights are fine-tuned for 100 epochs on the specific downstream task. We utilize ViT-Base as the backbone architecture, with a patch size of 16. The batch size for pre-training is typically set to 1024, unless stated otherwise, while for fine-tuning, it is set to 32. All experiments are conducted on four 32GB V100 GPUs, ensuring a fixed random seed for a fair comparison.

$k$  is set to 4 for the fine-spatial decoder, i.e., we double both the height and width of the reconstruction image. Other hyper-parameters and augmentations are set as recommended by the original papers [6] [7] [8].

3) *Evaluation Metrics:* To assess the effectiveness of our SSL model, we measure the performance of the fine-tuned weights on downstream tasks. The evaluation metrics employed in this study encompass Accuracy (Acc), Area under the ROC curve (AUC), and Average Precision (AP).

While both Linear Probing and Fine-tuning the whole model are commonly used for evaluation of learned SS representation [6] [8]. In this work, we only evaluate by fine-tuning as MAE learned representations are less linearly separable but strong non-linear features [8].

### B. Compare Original MAE on different pre-trained datasets

In order to determine the optimal datasets for pre-training, we conduct experiments using the original MAE [8] on four different combinations: CBIS-DDSM only, Lesion-Level datasets, and a combination of Lesion-Level and Image-Level datasets. The results are summarized in Table I. It is observed that utilizing all datasets with annotated lesion regions yields the best performance. However, when using datasets without lesion-level annotations and relying on random cropping from the mammograms, the performance on downstream tasks is

Method	Pre-trained Weights	Input	Acc	AP	AUC
Supervised	Random	224x224	50.3	53.0	79.0
	ImageNet		<b>67.2</b>	<b>73.0</b>	<b>90.0</b>
MAE [8]	ImageNet		61.8	68.0	88.0
	CBIS-DDSM		62.1	68.0	88.0
	Lesions Only		<b>66.0</b>	<b>71.0</b>	<b>90.0</b>
	MGs & Lesions		62.1	70.0	89.0

TABLE I: Pathology classification results on the CBIS-DDSM official test set when MAE is pre-trained on different datasets. (Except for the models pre-trained on ImageNet, which have been trained using a very large batch size in original works, the other experiments are pre-trained with a batch size of 1024)

negatively affected. We attribute this degradation to the imbalance between background crops and lesion crops in the training dataset, with a higher prevalence of background crops.

Although the performance of MAE using the pre-trained weights is significantly better than random initialization, it is still slightly lower compared to models pre-trained on ImageNet using supervised learning. This is expected as the available public MG datasets are relatively limited in size and have fewer annotations compared to the massive ImageNet dataset. Another factor that could contribute to the performance difference is the batch size used during pre-training. Original works on ImageNet often employ larger batch sizes, which can have an impact on the learned representations.

### C. Compare MIRAM with SOTA SSL algorithms

Table III provides a comparison between MIRAM and other state-of-the-art SSL methods in terms of pathology classification performance. In all experiments, the models are pre-trained using lesion-level datasets. MIRAM consistently outperforms DINO [7], Moco-v3 [6], and the original MAE [8]. Specifically, the *MIRAM-Standard* variant, which utilizes standard self-attention, achieves a 3% improvement in average precision (AP) and a 1% improvement in area under the ROC curve (AUC) compared to other SSL methods. These results demonstrate the effectiveness of our proposed multi-scale reconstruction pretext task.

In order to address the computational complexity of the high-resolution image reconstruction in MIRAM-Standard, we explore the use of recent linear self-attention methods, namely *Linformer* [12], *Performer* [13], and *Nystromformer* [14]. It is important to note that we only apply linear self-attention to the high-resolution decoder. Among these methods, Nystromformer demonstrates the best performance, maintaining the overall effectiveness of MIRAM. Furthermore, Nystromformer offers improved time and memory efficiency compared to the standard self-attention, as shown in Table II. Enhancing the efficiency of self-attention is crucial for scaling up our multi-scale pretext task, although it falls outside the scope of this paper.

Using linear self-attention to approximate standard self-attention is imperative to scale the idea of high-resolution image reconstruction. Table II compares the processing time and memory consumption between Nystromformer and standard self-attention.

	SSL Batch	GPU (GB)	Time to process 256 samples (s)
MIRAM-Standard	64	76	1.7952
MIRAM-Nystromformer	64	44	1.488
	128	68	1.1204
	256	124	0.9196

TABLE II: Comparison of the time and GPU RAM consumption between MIRAM using Nystromformer and MIRAM using Standard self-attention on  $224 \times 224$  images. Noting that when training with a batch size larger than 16, the Standard self-attention MIRAM encounters memory limitations, making it impossible to proceed.

	Input	SSL Batch	Acc.	AP	AUC
DINO [7]	112x112	1024	53.3	58.0	82.0
Moco-v3 [6]			60.2	65.0	86.0
MAE [8]			58.9	65.0	87.0
MIRAM-Standard (Ours)			<b>60.2</b>	<b>68.0</b>	<b>88.0</b>
MIRAM-Linformer (Ours)			59.0	66.0	87.0
MIRAM-Performer (Ours)			58.0	65.0	86.0
MIRAM-Nystromformer (Ours)			<b>61.0</b>	<b>67.0</b>	<b>87.0</b>

TABLE III: Pathology classification results of the proposed MIRAM on CBIS-DDSM official test set when compared with SOTA SSL methods.

### D. MIRAM on Mass Margins fine-grained classification task

We also evaluate MIRAM on the challenging task of mass margins multi-label classification. This task requires the model to capture subtle details of a mass lesion and make predictions for multiple labels. In multi-label problem, a lesion can belong to more than one class (e.g.: microlobulated and spiculated). Moreover, the available labels for fine-tuning on this downstream task are limited and highly imbalanced, posing additional challenges.

Despite the challenges posed by the fine-grained margin classification task, MIRAM exhibits significant improvements in performance. The macro AUC and macro AP metrics show a substantial increase of 2% and 4%, respectively, compared to the original MAE model (Tab. IV). These results highlight MIRAM’s ability to capture fine spatial details and validate the effectiveness of the proposed multi-scale reconstruction pretext task. Qualitative results are available in figure ??.

## V. CONCLUSION

In this work, we introduce a multi-scale reconstruction pretext task to enhance the generative SSL model for mammographic image analysis in risk assessment. We demonstrate that reconstructing multi-scale images leads to the learning of more effective features in our proposed MIRAM model. Furthermore, the reconstruction of high-resolution images enables the model to focus on finer spatial details. Through pre-training on diverse MG datasets, our approach consistently

	Input	SSL Batch	Macro AP	Macro AUC
MAE [8]	112x112	1024	31.0	64.0
MIRAM-Standard (Ours)			<b>35.0</b>	<b>66.0</b>

TABLE IV: Mass margins multi-label classification results of the proposed MIRAM on CBIS-DDSM official test set when compared with MAE.

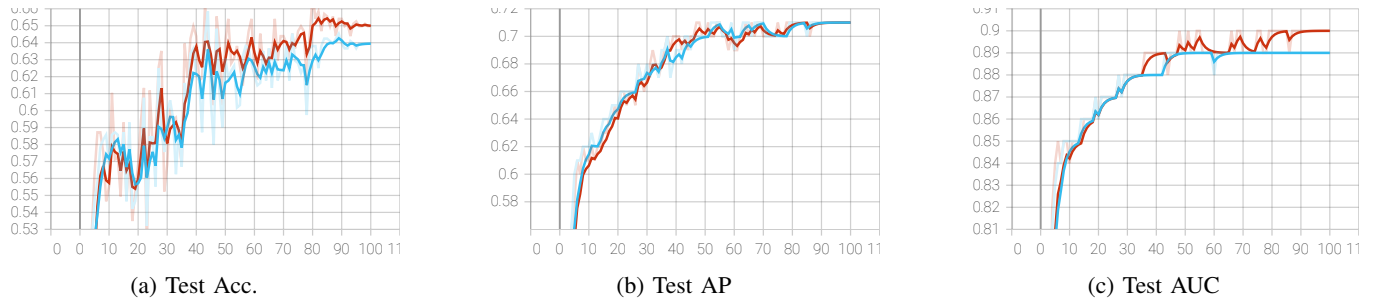


Fig. 3: Consistent pathology classification performance of proposed **MIRAM-Nystromformer** ( $224 \times 224$ ) on CBIS-DDSM official test set over 100 fine-tuning epochs: **Cyan** curve is for the original MAE, **Red** curve is for our proposed MAE.

Self-attention Block for second Decoder	Acc	AP	AUC
Linformer [12]	59.0	66.0	87.0
Performer [13]	58.0	65.0	86.0
Nystromformer [14]	<b>61.0</b>	67.0	87.0
Standard [11]	60.2	<b>68.0</b>	<b>88.0</b>

TABLE V: Performance of our proposed MAE using different Linear self-attention methods for pathology classification on CBIS-DDSM official test set ( $112 \times 112$ ). (Note that Linear self-attention is only used for the high-resolution decoder which is computationally expensive. For the original decoder, we use standard self-attention for all experiments)

outperforms strong SSL baselines in two breast cancer risk prediction tasks: pathology classification and mass margins classification.

## REFERENCES

- [1] S. Azizi *et al.*, “Big self-supervised models advance medical image classification,” in *Proceedings of the IEEE/CVF International Conference on Computer Vision*, 2021, pp. 3478–3488.
- [2] B. Li *et al.*, “Dual-stream multiple instance learning network for whole slide image classification with self-supervised contrastive learning,” in *Proceedings of the IEEE/CVF Conference on Computer Vision and Pattern Recognition*, 2021, pp. 14 318–14 328.
- [3] M. Tardy and D. Mateus, “Looking for abnormalities in mammograms with self-and weakly supervised reconstruction,” *IEEE Transactions on Medical Imaging*, vol. 40, no. 10, pp. 2711–2722, 2021.
- [4] S. Perek *et al.*, “Self supervised contrastive learning on multiple breast modalities boosts classification performance,” in *International Workshop on Predictive Intelligence In Medicine*. Springer, 2021, pp. 117–127.
- [5] J. D. Miller *et al.*, “Self-supervised deep learning to enhance breast cancer detection on screening mammography,” *arXiv preprint arXiv:2203.08812*, 2022.
- [6] X. Chen *et al.*, “An empirical study of training self-supervised vision transformers,” in *Proceedings of the IEEE/CVF International Conference on Computer Vision*, 2021, pp. 9640–9649.
- [7] M. Caron *et al.*, “Emerging properties in self-supervised vision transformers,” in *Proceedings of the IEEE/CVF International Conference on Computer Vision*, 2021, pp. 9650–9660.
- [8] K. He, X. Chen, S. Xie, Y. Li, P. Dollár, and R. Girshick, “Masked autoencoders are scalable vision learners,” in *Proceedings of the IEEE/CVF Conference on Computer Vision and Pattern Recognition*, 2022, pp. 16 000–16 009.
- [9] S. Khan *et al.*, “Transformers in vision: A survey,” *ACM Computing Surveys (CSUR)*, 2021.
- [10] A. Dosovitskiy *et al.*, “An image is worth 16x16 words: Transformers for image recognition at scale,” *arXiv preprint arXiv:2010.11929*, 2020.
- [11] A. Vaswani *et al.*, “Attention is all you need,” *Advances in neural information processing systems*, vol. 30, 2017.
- [12] S. Wang *et al.*, “Linformer: Self-attention with linear complexity,” *arXiv preprint arXiv:2006.04768*, 2020.
- [13] K. Choromanski *et al.*, “Rethinking attention with performers,” *arXiv preprint arXiv:2009.14794*, 2020.
- [14] Y. Xiong *et al.*, “Nyströmformer: A nystöm-based algorithm for approximating self-attention,” in *Proceedings of the... AAAI Conference on Artificial Intelligence. AAAI Conference on Artificial Intelligence*, vol. 35, no. 16. NIH Public Access, 2021, p. 14138.
- [15] I. C. Moreira *et al.*, “Inbreast: toward a full-field digital mammographic database,” *Academic radiology*, vol. 19, no. 2, pp. 236–248, 2012.
- [16] D. C. Moura *et al.*, “Benchmarking datasets for breast cancer computer-aided diagnosis (cadx),” in *Iberoamerican Congress on Pattern Recognition*. Springer, 2013, pp. 326–333.
- [17] R. S. Lee *et al.*, “A curated mammography data set for use in computer-aided detection and diagnosis research,” *Scientific data*, vol. 4, no. 1, pp. 1–9, 2017.
- [18] C. Matsoukas *et al.*, “Adding seemingly uninformative labels helps in low data regimes,” in *International Conference on Machine Learning*. PMLR, 2020, pp. 6775–6784.
- [19] L. Shen *et al.*, “Deep learning to improve breast cancer detection on screening mammography,” *Scientific reports*, vol. 9, no. 1, pp. 1–12, 2019.
- [20] M. Sorkhei *et al.*, “Csaw-m: An ordinal classification dataset for benchmarking mammographic masking of cancer,” *arXiv preprint arXiv:2112.01330*, 2021.
- [21] C. Cui *et al.*, “The chinese mammography database (cmmd): An online mammography database with biopsy confirmed types for machine diagnosis of breast,” *The Cancer Imaging Archive*, 2021.
- [22] D. Ribli *et al.*, “Detecting and classifying lesions in mammograms with deep learning,” *Scientific reports*, vol. 8, no. 1, pp. 1–7, 2018.